ACS NANO
Cite This: ACS Nano 2018, 12, 6079−6088
www.acsnano.org

ARTICLE

Ultra-Low-Power Smart Electronic Nose System Based on Three-Dimensional Tin Oxide Nanotube Arrays

Jiaqi Chen,[†] Zhuo Chen,[†] Farid Boussaid,[‡] Daquan Zhang,[†] Xiaofang Pan,[†,⊥] Huijuan Zhao,[§] Amine Bermak,[†,∥] Chi-Ying Tsui,[†] Xinran Wang,[§] and Zhiyong Fan*[,†]

[†]Department of Electronic and Computer Engineering, The Hong Kong University of Science and Technology, Clear Water Bay, Kowloon, Hong Kong SAR, China

[‡]Department of Electrical, Electronic and Computer Engineering, The University of Western Australia, Perth, WA 6009, Australia

[§]National Laboratory of Solid State Microstructure, School of Electronic Science and Engineering, and Collaborate Innovation Center of Advanced Microstructures, Nanjing University, Nanjing 210093, China

[∥]College of Science and Engineering, Hamad Bin Khalifa University, Doha, Qatar

Supporting Information

ABSTRACT: **In this work, we present a high-performance smart electronic nose (E-nose) system consisting of a multiplexed tin oxide (SnO_2) nanotube sensor array, read-out circuit, wireless data transmission unit, mobile phone receiver, and data processing application (App). Using the designed nanotube sensor device structure in conjunction with multiple electrode materials, high-sensitivity gas detection and discrimination have been achieved at room temperature, enabling a 1000 times reduction of the sensor's power consumption as compared to a conventional device using thin film SnO_2. The experimental results demonstrate that the developed E-nose can identify indoor target gases using a simple vector-matching gas recognition algorithm. In addition, the fabricated E-nose has achieved state-of-the-art sensitivity for H_2 and benzene detection at room temperature with metal oxide sensors. Such a smart E-nose system can address the imperative needs for distributed environmental monitoring in smart homes, smart buildings, and smart cities.**

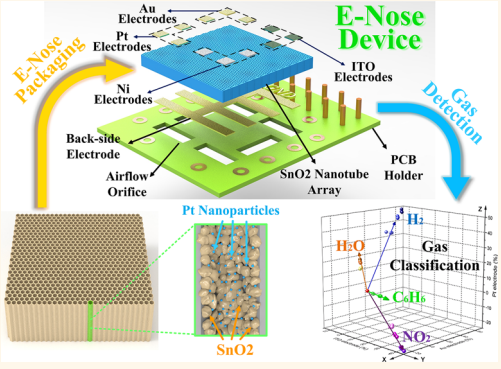

KEYWORDS: *tin oxide nanotube, low-power gas sensor, gas recognition, electronic nose, distributed sensor system*

Electronic noses (E-noses) are biomimetic devices mimicking the functionalities of mammals' olfaction system.[1,2] Employing chemical gas sensor arrays in conjunction with classification algorithms, smart E-noses are able to detect and discriminate types and concentrations of target gases.[3] E-noses have triggered enormous interest globally because of their critical roles in gas leakage detection, indoor air quality, and environmental safety monitoring.[4−8] This type of smart devices can be widely used in factories as well as smart homes and smart buildings, where the safety levels of particular gas species, such as hydrogen (H_2), carbon monoxide (CO), and nitrogen dioxide (NO_2), are well-defined either internationally or domestically.[9−11] In addition to monitoring fire hazardous gases, detection of low-level health-threatening chemical species (*e.g.*, benzene) emitted by house decorations and ventilation systems has also gained increasing attention over time in both developed and developing countries. This poses more sophisticated requirements for smart E-nose systems.[12]

As the primary purpose of E-noses is to ensure a safe environment for human users, E-noses should ideally be human-centered devices that can be either deployed in a distributed fashion around human users or integrated with the mobile/wearable devices of the users. Therefore, not only high performance but also ultra-low power consumption and miniaturized form are crucial.[13,14] In this regard, solid state semiconductor gas sensors are ideal candidates for this application. However, existing semiconductor E-nose technologies, such as microelectro-mechanical system (MEMS)-based micro-hot plates, microplatforms, *etc.*, all suffer from prohibitively high power consumption, *e.g.*, tens of milliwatts or even more, due to the utilization of resistive heaters to maintain a high operating temperature.[15,16] In addition, they are bulky,

Received: March 29, 2018
Accepted: May 24, 2018
Published: May 24, 2018

DOI: 10.1021/acsnano.8b02371
ACS Nano 2018, 12, 6079−6088

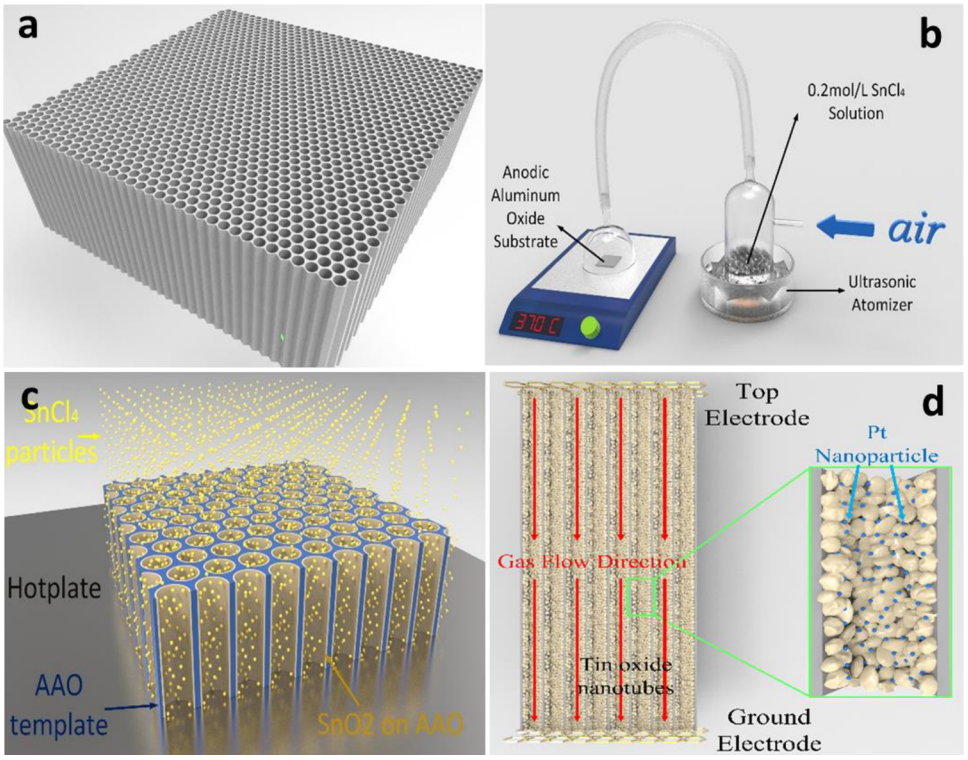

Figure 1. Illustration of the E-nose fabrication process and characterization. (a) Open-ended freestanding PAM. (b) USP setup. (c) Pyrolysis process of $SnCl_4$ on PAM. (d) Cross-section illustration of SnO_2 nanotubes after Pt decoration.

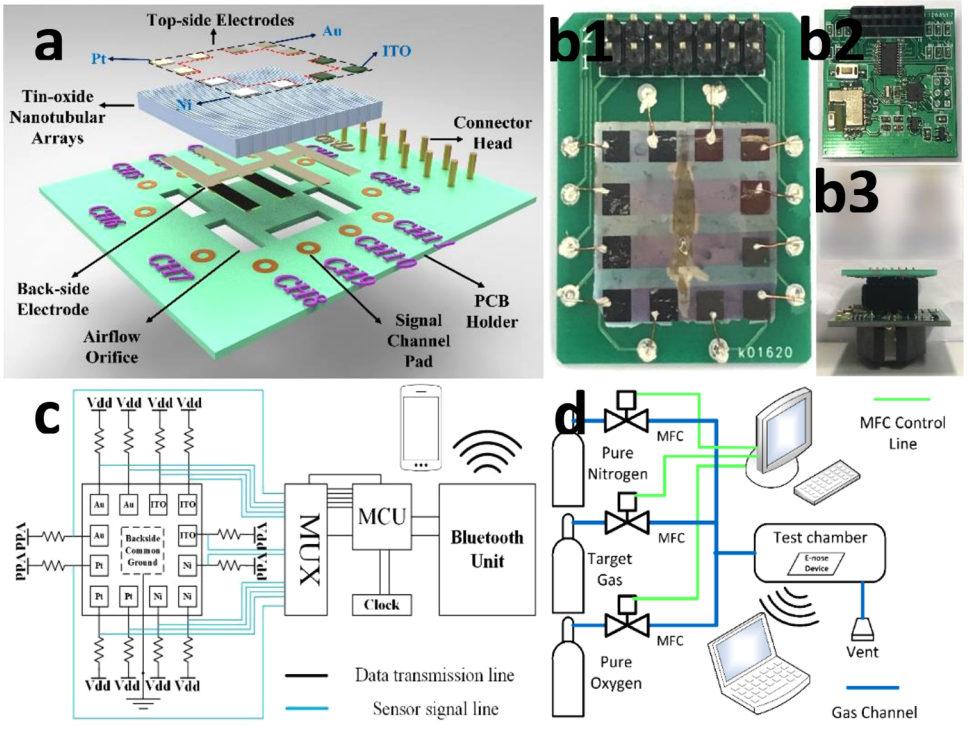

Figure 2. Illustration of E-nose and testing setup. (a) E-nose packaging structure. (b) Photograph of the sensor system. (c) Readout circuitry. (d) Experimental testing platform.

since the capacity of primary batteries has to be sufficiently large. Thus, they cannot be readily used as human-centered devices in the foreseeable future.[17] In this work, we demonstrate a high-performance solid state smart E-nose system using tin oxide (SnO_2) nanotube arrays as the key sensing material. The system also has a read-out electronic circuit, a wireless data transmission unit, a mobile phone receiver, and a data processing application (App). Using the proposed nanotube sensor device structure with a large surface area to interact with gas molecules, in conjunction with

DOI: 10.1021/acsnano.8b02371
ACS Nano 2018, 12, 6079−6088

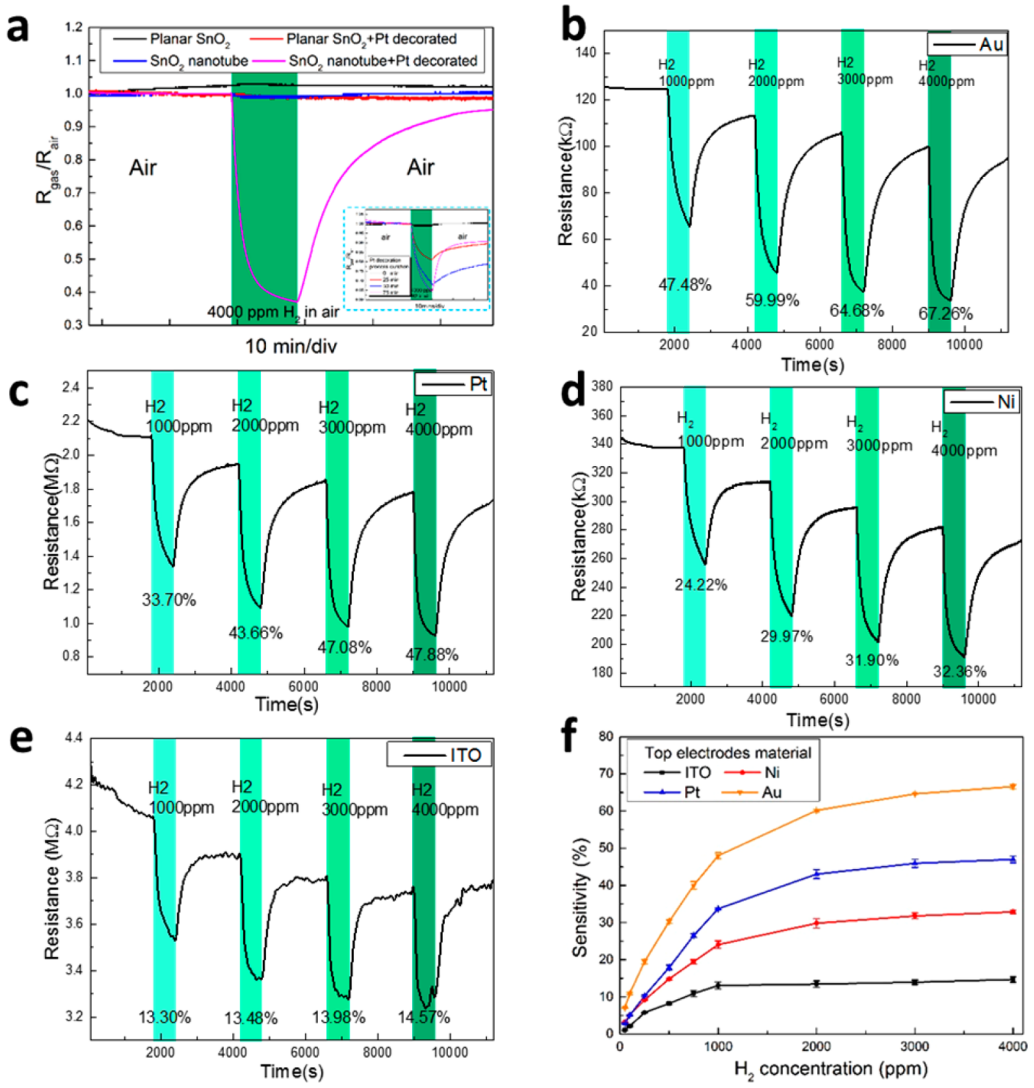

Figure 3. Test results of the E-nose toward hydrogen. (a) Performance of SnO_2 sensors on a planar substrate and PAM template with and without Pt decoration and responses for different Pt decoration times for SnO_2 sensors. (b) Sensitivity of E-nose for different H_2 concentrations. (c–f) Resistance changes of the E-nose for four different H_2 concentrations at room temperature. Repeatability of measurements for each sensor for three continuous cycles of 1000 ppm of H_2.

multiple electrode materials, high-sensitivity gas detection and discrimination have been achieved at room temperature. Therefore, sensor power consumption has been reduced by 3 orders of magnitude, as compared with a conventional device using thin film SnO_2. More specifically, the average power consumption of a heater-free single sensor device is around 12.5 μW, which represents 1% power of the state-of-the-art commercial SnO_2 sensors. Furthermore, the system gas-sensing test results demonstrate that the developed E-nose can identify indoor target gases using a simple vector-matching gas recognition algorithm. Particularly, the fabricated E-nose has achieved state-of-the-art sensitivity for hydrogen and benzene detection at room temperature for semiconductor gas sensors. Such a smart E-nose system can address the imperative need for distributed environmental monitoring in smart homes, smart buildings, and smart cities.

RESULTS AND DISCUSSION

E-Nose Sensor Fabrication. The fabrication process of the SnO_2 nanotube E-nose is illustrated in Figure 1, with more details provided in the Methods section. Briefly, to form a highly ordered nanotube array to enhance the surface-area-to-volume ratio (SA/V) of the sensing material, a 40 μm thick freestanding porous alumina membrane (PAM) with a 500 nm pitch and a 400 nm average pore size was fabricated (Figure 1a and Supplementary Figure S1a,b) using anodization of aluminum (Al) foil in conjunction with nanoimprinting.[18−20] The PAM was chosen as the host sensing material because it forms an insulating template capable of withstanding high temperatures during the fabrication process. It also offers a relatively good mechanical strength, which is crucial for future mass production.[21,22] After that, a 70 nm thick polycrystalline SnO_2 film with a ~70 nm grain size was deposited into the PAM using the ultrasonic spray pyrolysis (USP) method to form a SnO_2 nanotube array, as shown in Figure 1b and Supplementary Figure S1c.[23,24] We investigated the impact of the PAM pore diameter on device performance. A smaller pore diameter was found to translate into a larger surface area to volume ratio. However, if the pore diameter is too small, it becomes difficult to achieve conformal deposition of the

DOI: 10.1021/acsnano.8b02371
ACS Nano 2018, 12, 6079−6088

sensing material in the porous alumina membrane. A 400 nm pore diameter (before deposition) was found to be a good trade-off between performance and ease of fabrication. Notably, this process could be further used for depositing various types of other oxide materials in the PAM nanochannels. Subsequently, 5 nm diameter Pt nanoparticles were decorated on the entire surface of the SnO_2 nanotubes (Figure 1d and Supplementary Figure S1d) in colloidal solution; then four different materials including gold (Au), platinum (Pt), nickel (Ni), and indium tin oxide (ITO) were deposited on the top side of the SnO_2 nanotubes at different locations to form the top electrode array. A single layer of Au film was deposited on the bottom side of the SnO_2 nanotubes to form the common bottom electrodes. Figure 2a schematically shows the device structure, and Figure 2b1 shows a photograph of the actual device. Note that the USP method can highly conformally deposit a SnO_2 film into the nanochannels of the PAM with an aspect ratio higher than 100, as shown in Supplementary Figure S1c. This method has a high deposition rate and is much more cost-effective than other conformal coating techniques such as atomic layer deposition and chemical vapor deposition. The Pt nanoparticle decoration process is illustrated in Supplementary Figure S1d. Since the Pt particles are much smaller than the SnO_2 grains, they cannot be clearly distinguished in the SEM image. However, traces of the Pt element can be found in X-ray diffraction and energy-dispersive X-ray spectroscopy (EDS) analysis in the cross-section of the SnO_2 nanotubes (Supplementary Figure S2).

E-Nose Circuit Design and Power Consumption. The fabricated monolithically integrated sensor array was subsequently packaged on a printed circuit board (PCB), with the top electrode of each sensor connected to a signal channel pad, as shown in Figure 2a and b1. Note that the current size of each top electrode is 2 mm by 2 mm so that the resistance of each sensor is at the megaohm level, confirmed by the $I-V$ curves (Supplementary Figure S3). This size can be further reduced to increase sensor integration density and obtain devices with smaller dimensions in the future. The actual E-nose device consists of two PCBs as shown Figure 2b3. The upper PCB is the sensor PCB (Figure 2b1), and the lower is the data acquisition PCB, which comprises a multiplexer and a microcontroller unit (MCU) with an embedded analog-to-digital converter (Figure 2b2). A CR 2032 battery cassette is installed at the bottom of the device to provide a 3 V voltage. The detailed circuit design is provided in Supplementary Figure S4. During the gas-sensing test, the voltage drop (V_s) across each sensor is read-out by the MCU sequentially and the data are transmitted to the receiver through a Bluetooth unit (Figure 2c). The sensor resistance (R_s) can be simply calculated as

$$R_s = \frac{V_s}{V_{DD} - V_s} \times R_{const} \quad (1)$$

where R_{const} is the series resistance connected to the sensor. Our circuit level test shows that the entire E-nose system consumes 20 mW of power in a continuous working mode with all 12 sensors in operation. However, in four different types of sensors, only one sensor for each type is needed during operation. Thus, the power consumption of the four sensors is around 50 μW. This represents only 1% of a 2 × 2 state-of-the-art commercial SnO_2 sensor array (60 mW for 4 sensors) (Supplementary Table 1), which comprises embedded heaters to maintain the acquired high operating temperature. In addition, as the readout circuit can work under "sentry" mode with a low duty cycle of 1%, the average power consumption of our E-nose sensor system is only about 250 μW.

Hydrogen Gas Sensing. Figure 2d schematically shows our E-nose gas sensing test setup. Specifically, the target gas and balance gas are injected into the test chamber using computer-programmed mass flow controllers (MFCs) with a proper mixture ratio. The resistance change of the sensors is then measured by the MCU and transmitted to the receiver for data processing. More specifically, hydrogen gas (H_2) mixed with synthetic air was used to test the E-nose sensing performance since H_2 is one of the major flammable gases. To evaluate the effectiveness of the nanotube device structure and compare its sensing performance with its thin film counterpart, a 140 nm thick SnO_2 thin film was deposited on SiO_2-coated silicon wafers also using the USP process, and two Au electrodes were patterned on the thin film to fabricate a planar sensor device (Methods section). The test results of these two types of sensors for 4000 ppm of H_2 before and after Pt decoration are presented in Figure 3a. Interestingly, at room temperature both the SnO_2 nanotube sensor and the planar SnO_2 sensor do not respond to a low concentration of H_2. However, after Pt nanoparticle decoration, the SnO_2 nanotube sensor demonstrates a dramatically enhanced response to H_2, as compared with the Pt-decorated thin film sensor. Furthermore, Supplementary Figure S6a shows the nanotube sensor's response to H_2 with different Pt decoration times, indicating that a 75 min decoration time leads to the optimal sensing response. The thickness effect of the PAM has also been investigated, and 40 μm was found to exhibit the best sensitivity, as shown in Supplementary Figure S7. It is well known that at an elevated high temperature (200−300 °C) in air, SnO_2 shows a rise of conduction due to the reaction between H_2 and surface-adsorbed O_2, which forms neutral H_2O, thus releasing the trapped electrons back to SnO_2 from the surface-adsorbed O_2 molecules.[1,25] However, in our experiments carried out at room temperature, the reaction between H_2 and SnO_2 surface-adsorbed O_2 molecules is negligible; thus SnO_2 nearly demonstrates no conductance change upon exposure to H_2 gas. Nevertheless, Pt can significantly improve the SnO_2 sensing response to H_2 at room temperature mainly due to its catalytic behavior and reduction of the barrier height at the Pt/SnO_2 interface. More specifically, before the device was exposed to H_2, since Pt has a higher work function than SnO_2, electron depletion occurs in SnO_2 at the SnO_2/Pt interface, and a Schottky contact will be formed, as shown in Supplementary Figure S5. Such electron depletion certainly reduces the conductivity of the SnO_2 nanostructure. However, when H_2 is injected into the test chamber, H_2 molecules are readily adsorbed by the Pt nanoparticle surface and are then dissociated into atomic H on the surface of Pt. The H atoms contribute electrons to Pt, and the Schottky barrier height reduces after the H atoms rapidly diffuse through Pt reaching the Pt/SnO_2 interface, leading to an injection of electrons back to SnO_2 and to an increase of conductance of the SnO_2 nanotubes.[26,27]

Figure 3b−e demonstrate the response of the sensors using Au, Pt, Ni, and ITO top electrodes, respectively, toward hydrogen concentrations ranging from 1000 to 4000 ppm at room temperature. Note that 1000 ppm is the low detection limit for H_2 required by the U.S. Department of Energy, and 4000 ppm is the alarm level.[28] In general, it can be seen that

DOI: 10.1021/acsnano.8b02371
ACS Nano 2018, 12, 6079−6088

Table 1. Performance Comparison with Hydrogen Sensors

material	concentration	sensitivity	temperature	array size	ref
TiO_2-decorated SnO_2 nanoparticle	8000 ppm	17.4%	room temperature	2(separated)	39
Pd/Sn-decorated SnO_2 nanowire	5000 ppm	47.4%	room temperature	3(separated)	40
Pd nanowire	4000 ppm	3%	room temperature	2(separated)	41
Pd/Ni alloy thin film	1000 ppm	0.8%	room temperature	1	42
Pd/Cr nanowire network	1000 ppm	4%	room temperature	4(separated)	43
Pt−SnO_2 thin film	150 ppm	7%	85 °C	1	44
$Au_{0.5}Pd_{0.5}$ alloy thin film	100 ppm	2.5%	room temperature	1	45
Pt/SnO_2 nanoparticle	100 ppm	80%	350 °C	6(separated)	46
palladium nanowire	50 ppm	0.4%	room temperature	1	47
Pt nanowire	50 ppm	0.8%	270 °C	4(separated)	48
palladium nanowire	50 ppm	1%	room temperature	2(separated)	49
palladium film	50 ppm	2%	room temperature	1	50
Pt-decorated SnO_2 nanotube	50 ppm	7%	room temperature	4 × 3(integrated)	this work
	100 ppm	11%			
	1000 ppm	47%			
	4000 ppm	67%			

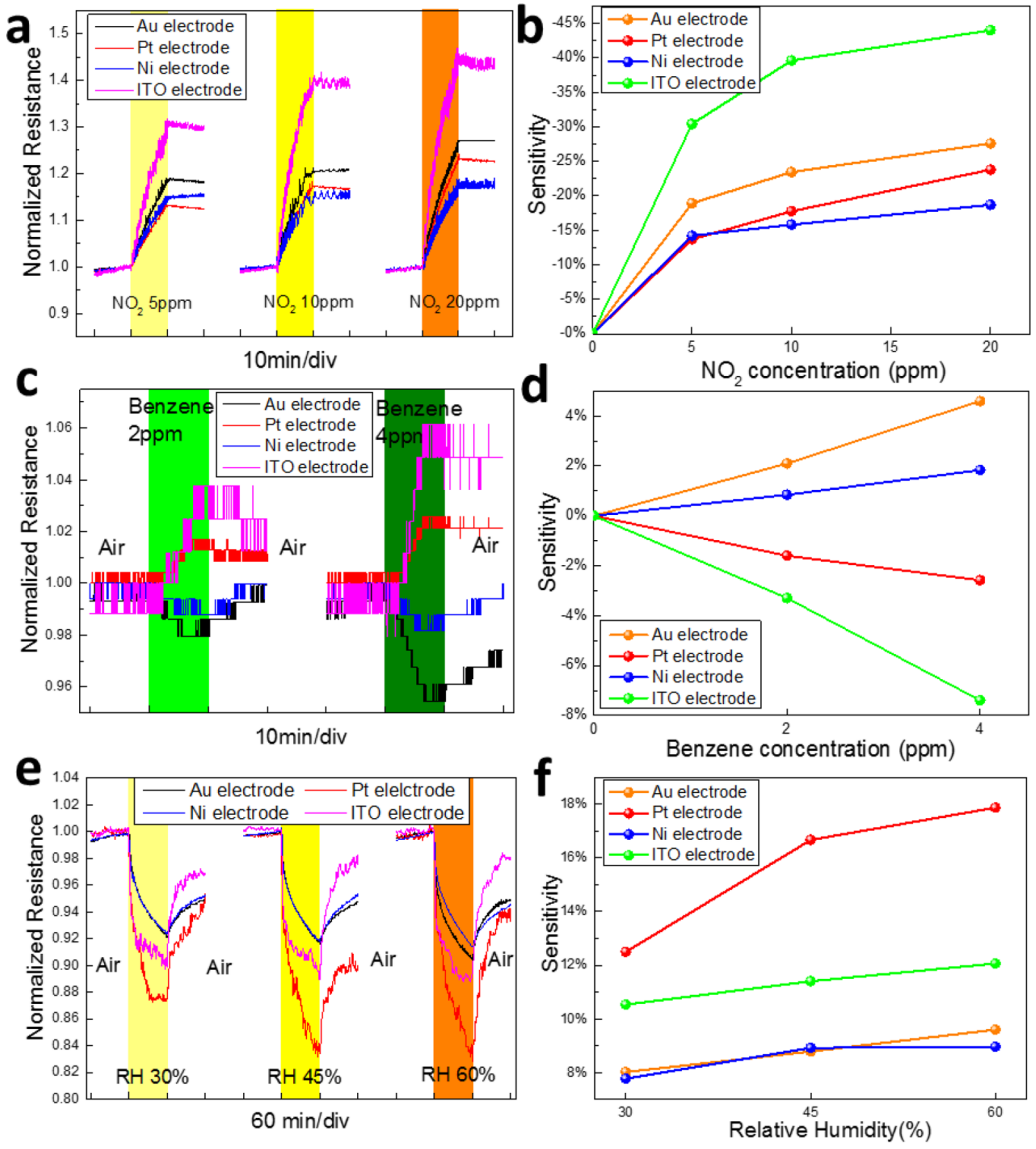

Figure 4. Test results of the E-nose toward nitrogen dioxide, benzene, and humidity. (a, c, e) E-nose response toward different concentrations of NO_2, benzene, and relative air humidity at room temperature. (b, d, f) Sensitivity curves of the E-nose for NO_2, benzene, and relative humidity.

DOI: 10.1021/acsnano.8b02371
ACS Nano 2018, 12, 6079−6088

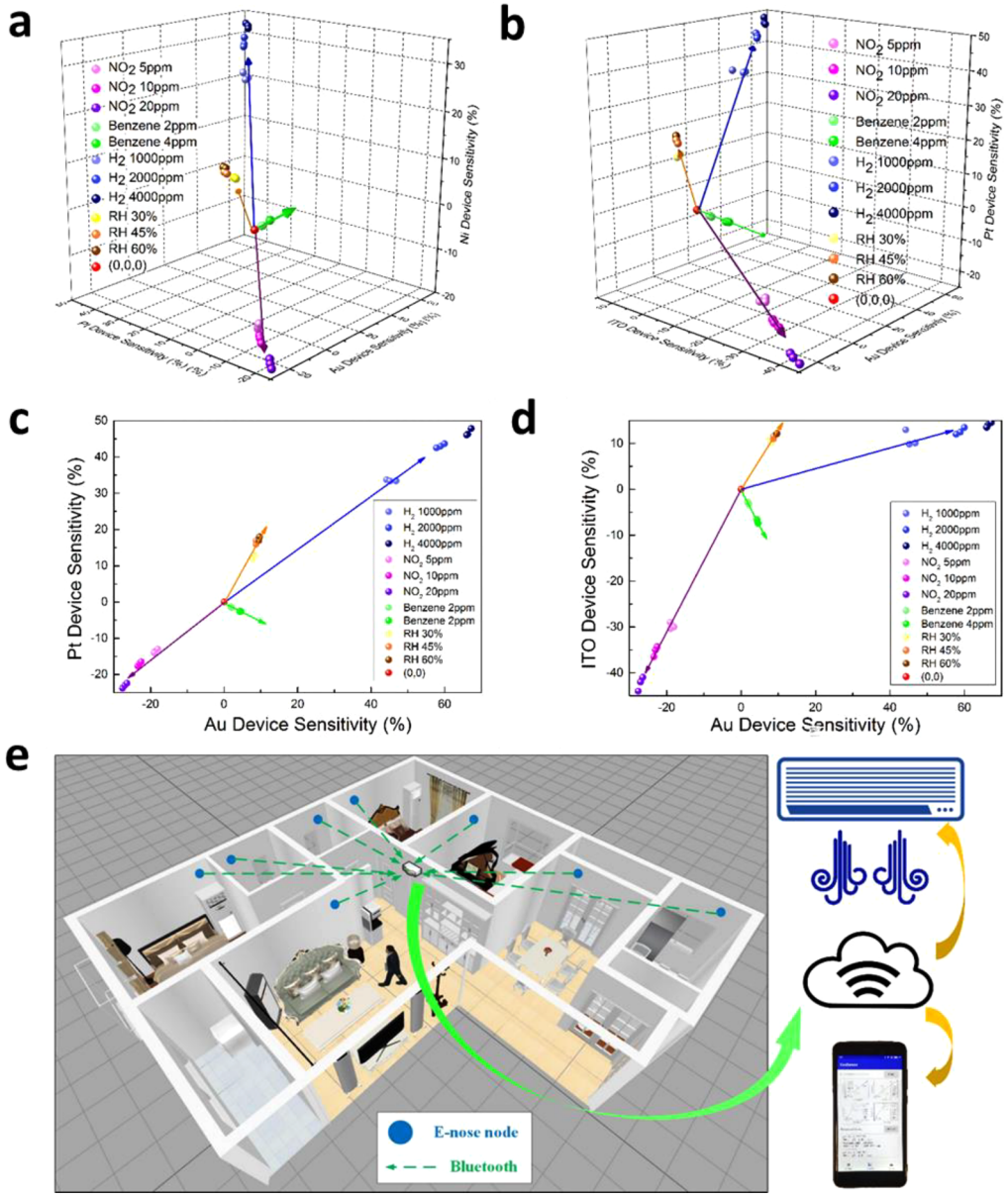

Figure 5. Distinguishing ability of the E-nose and illustration of the E-nose in an indoor application. (a and b) LVQ method for gas classification in cubic maps. (c and d) Top views of corresponding cubic maps. (e) Illustration of the proposed E-nose application in future smart buildings.

higher H_2 concentrations lead to larger sensor resistance changes. To perform a more quantitative analysis, the sensitivity of a given sensor to a target gas is defined as

$$\text{Sensitivity} = \frac{R_O - R_{Gas}}{R_O} \times 100\% \quad (2)$$

where R_O is the transient resistance before H_2 injection and R_{Gas} is the resistance at the end of the 10 min H_2 injection period. The test results show that for 4000 ppm of H_2 the sensitivities of sensors with Au, Pt, Ni, and ITO electrodes are 67.26%, 47.88%, 32.36%, and 14.57%, respectively. Supplementary Figure S8 reports additional sensor response to 1000 ppm of H_2 and shows less than a 3% sensitivity shift with excellent repeatability for all devices. Lower H_2 concentrations ranging from 750 ppm down to 10 ppm were also used for sensing test, with the responses provided in Supplementary Figure S9 and Figure S6b. Notably, although the sensors demonstrated a readable response toward H_2 below 10 ppm (signal-to-noise ratio (SNR) = 2), our existing MFCs do not allow for an accurate control of gas concentration below 10 ppm. As the result, 10 ppm is the lowest concentration we could actually measure. However, the lower limit could be further reduced by using an MFC with a smaller flow rate range. Nevertheless, 50 ppm of H_2 detection at room temperature with a semiconductor sensor provides already the state-of-the-art detection capability in atmospheric pressure. The calculated sensitivities at different H_2 concentrations are plotted in Figure 3f and Supplementary Figure S6. The overall trend shows higher sensitivity can be achieved with higher gas concentration with an exponential dependence on concentration that agrees with the empirical formula for metal oxide gas sensors (Supporting Information). The performance of our nanotube sensor was benchmarked against previously reported H_2 sensors in Table 1. It can be seen that among all room-

DOI: 10.1021/acsnano.8b02371
ACS Nano 2018, 12, 6079−6088

temperature-operated sensors our nanotube sensor demonstrates the best sensitivity for H_2 concentrations ranging from 4000 to 100 ppm. Although the Pt/SnO_2 nanoparticle sensor shows higher sensitivity to 100 ppm of H_2, it requires a 350 °C operating temperature and high power consumption.

Nitrogen Dioxide and Benzene Gas Sensing. In addition to flammable H_2 gas sensing, detection of toxic NO_2 and benzene gases with nanotube sensors has also been examined. Note that NO_2 is one typical kind of air pollution from automobile exhaust emission, while benzene can be emitted by house/building construction/decoration materials. Figure 4a reports nanotube sensor responses toward oxidizing NO_2 for three different indoor level concentrations (5, 10, and 20 ppm) in synthetic air and at room temperature. Figure 4b reveals the exponential dependence of sensitivity *versus* NO_2 concentration. It can be seen that exposure to NO_2 increases sensor resistance since NO_2 molecules can withdraw electrons from metal oxides.[29,30] The ITO electrode sensor exhibits the largest resistance change because of the affected work function and barrier height of the interface. However, given that NO_2 is a strong oxidizing gas, the recovery process of the E-nose at room temperature usually takes hours to recover back to the original baseline resistances. Although a heater or a UV LED could be used to help the recovery,[1,31] such a heater or LED would only need to be turned on when a dangerous level of NO_2 has been detected. In real life applications, due to the rare opportunity of detecting high-concentration NO_2, the heater would remain off for most of the time. The use of a heater only for fast sensor recovery will thus result in a significantly lower power budget as compared to commercial sensors using heaters for high-temperature operation.

Figure 4c shows the E-nose's response to benzene. Because of the low concentration (2−4 ppm) and room-temperature operation, acquired responses were relatively small compared to the sensitivity toward H_2, leading to low signal-to-noise ratio in the response curve. However, the sensitivity could still be clearly observed and calculated from test results, as presented in Figure 4d. Intriguingly, for the ITO and Pt electrode sensors, benzene acts as an oxidizing gas, while it acts as a reducing gas for Au and Ni electrode sensors. Figure 4d plots the sensitivity *versus* benzene concentration where the four normalized resistance curves distinctively show positive and negative responses. The fact that ITO and Pt electrode sensors show a negative response, while Ni and Au electrode sensors show a positive response can be attributed to the different effect on electrode work function exerted by benzene, leading to a change of contact property, *e.g.*, barrier height, between the electrodes and sensing material. Meanwhile, the catalytic effect of the electrode material toward the target gas can also affect the impedance of the sensor.[32] It is noteworthy to point out that 8% sensitivity for the ITO electrode sensor (Figure 4d) is, to our best our knowledge, the highest sensitivity of a SnO_2-based gas sensor toward indoor levels of benzene at room temperature.[33,34] In contrast to NO_2 and H_2, individual sensors of the E-nose exhibit different sensing properties when exposed to benzene. This can be further exploited for subsequent gas identification tasks. The impact of humidity on sensors was also evaluated for 30%, 45%, and 60% relative humidity. Among the four types of sensors, the Pt electrode sensor exhibits the highest sensitivity to humidity because water molecules could be more easily dissociated into hydroxyl species on the Pt electrodes.[35] By changing the barrier height of the Schottky contact and donating free electrons, the resistance of SnO_2 nanotubes with Pt electrodes shows a large reduction, as shown in Figure 4e and f. Note that the sensor array could recover back toward its original baseline even at room temperature.

Gas Identification Algorithm Design. The above E-nose tests revealed that each type of sensor has a characteristic response pattern to a specific gas. This behavior can be used for subsequent gas identification. Learning vector quantization (LVQ) is used to process acquired data and identify the sensed gas.[36] With the previous input training data defining the training vectors, the new testing data are also labeled as testing vectors and then discriminated by comparing with training data. Based on acquired data, a small library without a dimensionality reduction process is presented in Figure 5a,b. Note that the axes represent the sensitivity as defined in eq 2, and there is no overlap between the sensitivity patterns representing each gas signature, with each gas having their own cluster direction. When applying the LVQ method for gas identification, there will not be any cluster overlap even if the identification zone of sensitivity is set at ±3%. This means the E-nose can accurately distinguish among all four target gases. To better visualize the LVQ classification, two-dimensional coordinates representing the top view of Figure 5a,b are drawn in Figure 5c,d, with parameters labeled in each vector. The other two sets of combinations are presented in Supplementary Figure S10. Clearly, the vector orientation is the signature of a given gas type. Therefore, in practice, when an unknown gas is sensed by the E-nose, the orientation and length of the acquired vector associated with its sensitivity pattern can be obtained and subsequently matched with the vectors prestored in the identification library. Based on eq 3 and the vector length, the concentration of the identified gas could be calculated, which means this vector representation method provides a wide discrimination range for these gases.[37,38] C_g in eq 3 stands for the concentration (ppm) of the target gas, which is linearly related with the partial pressure (P_g). S is the sensitivity calculated from the sensor array. A_g and the exponent coefficient, α, depend on the analyte and electrode materials, which has already been trained and stored in the library.

$$C_g = 10^6 \times P_g = 10^6 \times \left(\frac{S}{(1 - S) \times A_g} \right)^{1/\alpha} \quad (3)$$

As our E-nose is a miniaturized, portable, and low-power device, we have built an in-house sensor network consisting of multiple E-noses and a mobile phone receiver with a software App developed for data processing. The supplementary video shows a town gas leakage detection scenario, in which hydrogen is the major component (50%), with our wireless E-nose. Fast response to hydrogen in a town gas released by a kitchen stove is demonstrated. Figure 5e illustrates the concept of deploying our lower power E-nose system in a smart home as an environmental safety system. Owing to the long operation lifetime and wireless communication, the sensor nodes could be distributed to any preferred location within Bluetooth broadcasting range (*e.g.*, 100 m). The acquired data can be in fact transmitted to a server and then uploaded to the Cloud. The residents of the house can monitor the environment in the house anywhere with the Internet. If the system is connected with air conditioners or air purifiers, the system could also trigger air purification/exchange automatically.

DOI: 10.1021/acsnano.8b02371
ACS Nano 2018, 12, 6079−6088

CONCLUSIONS

In summary, we reported a high-performance ultra-low-power E-nose system based on highly ordered SnO_2 nanotube arrays. The proposed nanotubes have a high SA/*V* and Pt decoration to significantly improve sensor performance. The E-nose demonstrates a heater-free detection capability toward H_2, NO_2, benzene, and humidity, with only 1% of power consumption of a commercial SnO_2 thin film gas sensor. Particularly, the E-nose has achieved state-of-the-art H_2 and benzene detection sensitivity. Benefitting from multiple types of electrodes, the monolithically integrated sensor array has successfully distinguished different gases using a simple vector quantization algorithm. With its readout circuit, the E-nose can transmit sensing data through a Bluetooth unit, to a mobile phone receiver, which enables construction of high-performance smart sensor networks. Overall, the ultra-low-power smart E-nose system reported here can thus play a critical role in future smart homes and buildings.

METHODS

Experimental Methods. *Freestanding Open-Ended PAM Substrate Fabrication.* A 0.5 mm thick aluminum foil was cut into a 2 × 2 cm^2 square piece, which was placed in an ultrasonic bath of acetone, followed by a 2-propanol bath. The aluminum foil was then rinsed with deionized water. After that, it was put into an electrical polishing solution ($HClO_4/C_2H_5OH$, 1:3 in volume ratio) under a 16 V positive voltage for 2 min. The polished Al foil was then immersed in an anodizing solution ($H_2O/C_2H_6O_2$/85% H_3PO_4, 200:100:1 in volume ratio) with a 200 V voltage applied between the Al foil and the negative carbon electrode. When the thickness of the PAM film reached 40 μm, the entire foil was immersed in a 0.2 mol/L H_3PO_4 solution. A positive bias voltage of 200 V was applied on the aluminum foil through a programmed Keithley, and then the Al foil was switched to constant-current mode (4 mA) until the bias voltage dropped to 4 V. The edge of the foil was then manually scratched with a knife. Electrical polishing was then used again to separate the interface of aluminum from the PAM under a 16 V voltage for 3 min. After the polishing process and natural drying, two freestanding PAM membranes could be detached from the Al foil by tweezers. To remove the barrier layer, the membranes were immersed into a 5% H_3PO_4 solution placed in a 53 °C water bath for 35 min.

SnO_2 Deposition on a Freestanding PAM Template. A 0.2 mol/L $SnCl_4{\cdot}5H_2O$ ethanol solution was used as the precursor solution for the USP process. After vibrating it into a vapor phase in a container using an ultrasonic atomizer, the precursor was carried into a nozzle by controlled dry air. The PAM template in the nozzle was heated to 370 °C for the subsequent spray pyrolysis process. Because of the open-ended structure, a 17 min spray pyrolysis process was conducted on each side of the PAM template. For the planar comparison test, the same precursor solution (0.2 mol/L $SnCl_4{\cdot}5H_2O$ ethanol solution) was used for depositing SnO_2 on 1 μm oxide coated silicon wafer. The deposition process on the wafer was conducted for 34 min.

Pt Decoration and Forming Sensor Array. After the USP process, the nanotube array was immersed in a 0.5 wt % Pt particle (5 nm diameter) solution for surface decoration with a 600 rpm stirring rate. Following the decoration process, the freestanding SnO_2 nanotube array was covered by a shadow mask with 12 2 × 2 mm^2 square openings. Then, 100 nm thick Au, Pt, Ni, and ITO were thermally evaporated each time to three neighboring openings, respectively, forming the electrode array shown in Figure 2a. The backside of the SnO_2 nanotube array was covered by a shadow mask with a fish bone shaped opening before 100 nm thick Au was evaporated to form the common ground.

E-Nose Characterization Procedure. The E-nose system, integrated with a readout circuit, was put inside a glass chamber. Three program-controlled MFCs (UNIT Instrument, model UFC-8100) were connected to the target gases, pure nitrogen, and pure oxygen, respectively. In our work, three types of target gases balanced in nitrogen were used, namely, 5000 ppm of H_2, 25 ppm of NO_2, and 5 ppm of benzene. The concentration of the mixed gas delivered to gas sensors was controlled through the MFC flow rate ratios. The total flow rate was always maintained at 500.

ASSOCIATED CONTENT

Supporting Information

The Supporting Information is available free of charge on the ACS Publications website at DOI: 10.1021/acsnano.8b02371.

Methods and additional figures (PDF)

Demo video for ultra-low-power smart electronic nose system (AVI)

AUTHOR INFORMATION

Corresponding Author

*Tel (Z. Fan): +852-23588027. E-mail: eezfan@ust.hk.

ORCID

Xinran Wang: 0000-0002-3975-1667

Zhiyong Fan: 0000-0002-5397-0129

Present Address

⊥College of Information Engineering, Shenzhen University, Shenzhen, Guangdong, China.

Author Contributions

J.C., Z.C., F.B., X.P., A.B., C.Y.T., X.W., and Z.F. designed the experiments. J.C., Z.C., D.Z., H.Z, and Z.F. carried out the experiments. J.C., Z.C., F.B., and Z.F. contributed to data analysis. J.C., F.B., X.W., and Z.F. wrote and revised the paper, and all authors provided feedback.

Notes

The authors declare no competing financial interest.

ACKNOWLEDGMENTS

This work was supported by National Natural Science Foundation of China (project 51672231), General Research Fund (16237816) from Hong Kong Research Grant Council, ITS/415/16 and ITS/211/16FP from Hong Kong Innovation Technology Commission, and the Australian Research Council Discovery Projects funding scheme (Project DP130104374). The authors also acknowledge the support from the Center for 1D/2D Quantum Materials and State Key Laboratory on Advanced Displays and Optoelectronics at HKUST.

REFERENCES

(1) Carpenter, M. A.; Mathur, S.; Kolmakov, A. *Metal Oxide Nanomaterials for Chemical Sensors*; Springer Science & Business Media, 2012.

(2) Persaud, K.; Dodd, G. Analysis of Discrimination Mechanisms in the Mammalian Olfactory System Using a Model Nose. *Nature* **1982**, *299*, 352−355.

(3) Scott, S. M.; James, D.; Ali, Z. Data Analysis for Electronic Nose Systems. *Microchim. Acta* **2006**, *156*, 183−207.

(4) Chen, K.; Gao, W.; Emaminejad, S.; Kiriya, D.; Ota, H.; Nyein, H. Y. Y.; Takei, K.; Javey, A. Printed Carbon Nanotube Electronics and Sensor Systems. *Adv. Mater.* **2016**, *28*, 4397−4414.

(5) Pan, Z. W.; Dai, Z. R.; Wang, Z. L. Nanobelts of Semiconducting Oxides. *Science* **2001**, *291*, 1947−1949.

(6) Zampolli, S.; Elmi, I.; Ahmed, F.; Passini, M.; Cardinali, G. C.; Nicoletti, S.; Dori, L. An Electronic Nose Based on Solid State Sensor Arrays for Low-Cost Indoor Air Quality Monitoring Applications. *Sens. Actuators, B* **2004**, *101*, 39−46.

DOI: 10.1021/acsnano.8b02371
ACS Nano 2018, 12, 6079−6088

(7) Nagle, H. T.; Gutierrez-Osuna, R.; Schiffman, S. S. the How and Why of Electronic Noses. *IEEE Spectrum* **1998**, *35*, 22−31.
(8) Lee, D. S.; Lee, D. D.; Ban, S. W.; Lee, M.; Kim, Y. T. SnO_2 Gas Sensing Array for Combustible and Explosive Gas Leakage Recognition. *IEEE Sens. J.* **2002**, *2*, 140−149.
(9) Prosser, S. J.; Schmidt, E. D. Smart Sensors for Industrial Applications. *Sens. Rev.* **1997**, *17*, 217−222.
(10) Lewis, F. L. Wireless Sensor Networks. *Smart environments: technologies, protocols, and applications* **2005**, 11−46.
(11) Sysoev, V. V.; Button, B. K.; Wepsiec, K.; Dmitriev, S.; Kolmakov, A. Toward The Nanoscopic "Electronic Nose": Hydrogen vs Carbon Monoxide Discrimination With an Array of Individual Metal Oxide Nano-and Mesowire Sensors. *Nano Lett.* **2006**, *6*, 1584−1588.
(12) Orwell, R. L.; Wood, R. L.; Tarran, J.; Torpy, F.; Burchett, M. D. Removal of Benzene by the Indoor Plant/Substrate Microcosm and Implications for Air Quality. *Water, Air, Soil Pollut.* **2004**, *157*, 193−207.
(13) McAlpine, M. C.; Ahmad, H.; Wang, D.; Heath, J. R. Highly Ordered Nanowire Arrays on Plastic Substrates for Ultrasensitive Flexible Chemical Sensors. *Nat. Mater.* **2007**, *6*, 379.
(14) Hong, H. K.; Shin, H. W.; Yun, D. H.; Kim, S. R.; Kwon, C. H.; Lee, K.; Moriizumi, T. Electronic Nose System with Micro Gas Sensor Array. *Sens. Actuators, B* **1996**, *36*, 338−341.
(15) Kim, I.; Choi, W. Y. Hybrid Gas Sensor Having TiO_2 Nanotube Arrays and SnO_2 Nanoparticles. *Int. J. Nanotechnol.* **2017**, *14*, 155−165.
(16) Guo, B.; Bermak, A.; Chan, P. C.; Yan, G. Z. Characterization of Integrated Tin Oxide Gas Sensors With Metal Additives and Ion Implantations. *IEEE Sens. J.* **2008**, *8*, 1397−1398.
(17) Ha, M.; Park, J.; Lee, Y.; Ko, H. Triboelectric Generators and Sensors for Self-Powered Wearable Electronics. *ACS Nano* **2015**, *9*, 3421−3427.
(18) Fan, Z.; Razavi, H.; Do, J. W.; Moriwaki, A.; Ergen, O.; Chueh, Y. L.; Neale, S.; Javey, A. Three-Dimensional Nanopillar-Array Photovoltaics on Low-Cost and Flexible Substrates. *Nat. Mater.* **2009**, *8*, 648−653.
(19) Lin, Q.; Hua, B.; Leung, S. F.; Duan, X.; Fan, Z. Efficient Light Absorption with Integrated Nanopillar/Nanowell Arrays for Three-Dimensional Thin-Film Photovoltaic Applications. *ACS Nano* **2013**, *7*, 2725−2732.
(20) Leung, S. F.; Yu, M.; Lin, Q.; Kwon, K.; Ching, K. L.; Gu, L.; Fan, Z. Efficient Photon Capturing with Ordered Three-Dimensional Nanowell Arrays. *Nano Lett.* **2012**, *12*, 3682−3689.
(21) Fan, Z.; Ruebusch, D. J.; Rathore, A. A.; Kapadia, R.; Ergen, O.; Leu, P. W.; Javey, A. Challenges and Prospects of Nanopillar-based Solar Cells. *Nano Res.* **2009**, *2*, 829−843.
(22) Tavakoli, M. M.; Lin, Q.; Leung, S. F.; Lui, G. C.; Lu, H.; Li, L.; Xiang, B.; Fan, Z. Efficient, Flexible and Mechanically Robust Perovskite Solar Cells on Inverted Nanocone Plastic Substrates. *Nanoscale* **2016**, *8*, 4276−4283.
(23) Park, S. H.; Son, Y. C.; Willis, W. S.; Suib, S. L.; Creasy, K. E. Tin Oxide Films Made by Physical Vapor Deposition-Thermal Oxidation and Spray Pyrolysis. *Chem. Mater.* **1998**, *10*, 2389−2398.
(24) Hieda, K.; Hyodo, T.; Shimizu, Y.; Egashira, M. Preparation of Porous Tin Dioxide Powder by Ultrasonic Spray Pyrolysis and Their Application to Sensor Materials. *Sens. Actuators, B* **2008**, *133*, 144−150.
(25) Al-Hardan, N. H.; Abdullah, M. J.; Aziz, A. Sensing Mechanism of Hydrogen Gas Sensor Based on RF-Sputtered Zno Thin Films. *Int. J. Hydrogen Energy* **2010**, *35*, 4428−4434.
(26) Lim, W.; Wright, J. S.; Gila, B. P.; Pearton, S. J.; Ren, F.; Lai, W. T.; Chen, L. C.; Hu, M. S.; Chen, K. H. Selective-Hydrogen Sensing at Room Temperature with Pt-Coated Inn Nanobelts. *Appl. Phys. Lett.* **2008**, *93*, 202109.
(27) Cerchez, M.; Langer, H.; El Achhab, M.; Heinzel, T.; Ostermann, D.; Lüder, H.; Degenhardt, J. Dynamics of Hydrogen Sensing with Pt/TiO_2 Schottky Diodes. *Appl. Phys. Lett.* **2013**, *103*, 033522.
(28) Buttner, W.; Burgess, R.; Post, M.; Rivkin, C. *Summary and Findings from the NREL/DOE Hydrogen Sensor Workshop*; National Renewable Energy Laboratory: Golden, CO, 2011, NREL/TP-5600-55645. www.nrel.gov/docs/fy12osti/55645.pdf (date of access: 05/10/2018).
(29) Fan, Z.; Lu, J. G. Gate-refreshable Nanowire Chemical Sensors. *Appl. Phys. Lett.* **2005**, *86*, 123510.
(30) Pan, X.; Liu, X.; Bermak, A.; Fan, Z. Self-Gating Effect Induced Large Performance Improvement of ZnO Nanocomb Gas Sensors. *ACS Nano* **2013**, *7*, 9318−9324.
(31) Kong, J.; Franklin, N. R.; Zhou, C.; Chapline, M. G.; Peng, S.; Cho, K.; Dai, H. Nanotube Molecular Wires as Chemical Sensors. *Science* **2000**, *287*, 622−625.
(32) Rank, S.; Hafner, S.; Barsan, N.; Weimar, U. the Impact of the Nature of the Electrode Material on SnO_2 Thick Film Sensor Performance: Influence on Oxygen Adsorption. *Procedia Eng.* **2012**, *47*, 514−517.
(33) Stuckert, E. P.; Miller, C. J.; Fisher, E. R. the Effect of Ar/O_2 and H_2O Plasma Treatment of SnO_2 Nanoparticles and Nanowires on Carbon Monoxide and Benzene Detection. *ACS Appl. Mater. Interfaces* **2017**, *9*, 15733−15743.
(34) Zito, C. A.; Perfecto, T. M.; Volanti, D. P. Impact of Reduced Graphene Oxide on the Ethanol Sensing Performance of Hollow SnO_2 Nanoparticles Under Humid Atmosphere. *Sens. Actuators, B* **2017**, *244*, 466−474.
(35) Michaelides, A.; Hu, P. A Density Functional Theory Study of Hydroxyl and the Intermediate in the Water Formation Reaction on Pt. *J. Chem. Phys.* **2001**, *114*, 513−519.
(36) Kohonen, T. The Self-Organizing Map. *Neurocomputing* **1998**, *21*, 1−6.
(37) Scott, R. W.; Yang, S. M.; Chabanis, G.; Coombs, N.; Williams, D. E.; Ozin, G. A. Tin Dioxide Opals and Inverted Opals: Near-Ideal Microstructures for Gas Sensors. *Adv. Mater.* **2001**, *13*, 1468−1472.
(38) Yin, Y. X.; Jiang, L. Y.; Wan, L. J.; Li, C. J.; Guo, Y. G. Polyethylene Glycol-Directed SnO_2 Nanowires for Enhanced Gas-Sensing Properties. *Nanoscale* **2011**, *3*, 1802−1806.
(39) Nasirian, S.; Moghaddam, H. M. Polyaniline Assisted by TiO_2: SnO_2 Nanoparticles as a Hydrogen Gas Sensor at Environmental Conditions. *Appl. Surf. Sci.* **2015**, *328*, 395−404.
(40) Jeong, S. H.; Kim, S.; Cha, J.; Son, M. S.; Park, S. H.; Kim, H. Y.; Cho, M. H.; Whangbo, M. H.; Yoo, K. H.; Kim, S. J. Hydrogen Sensing Under Ambient Conditions Using SnO_2 Nanowires: Synergetic Effect of Pd/Sn Co-Deposition. *Nano Lett.* **2013**, *13*, 5938−5943.
(41) Yang, F.; Taggart, D. K.; Penner, R. M. Fast, Sensitive Hydrogen Gas Detection Using Single Palladium Nanowires that Resist Fracture. *Nano Lett.* **2009**, *9*, 2177−2182.
(42) Hughes, R. C.; Schubert, W. K. Thin Films of Pd/Ni Alloys for Detection of High Hydrogen Concentrations. *J. Appl. Phys.* **1992**, *71*, 542−544.
(43) Zeng, X. Q.; Wang, Y. L.; Deng, H.; Latimer, M. L.; Xiao, Z. L.; Pearson, J.; Xu, T.; Wang, H. H.; Welp, U.; Crabtree, G. W.; Kwok, W. K. Networks of Ultrasmall Pd/Cr Nanowires as High Performance Hydrogen Sensors. *ACS Nano* **2011**, *5*, 7443−7452.
(44) Rane, S.; Arbuj, S.; Rane, S.; Gosavi, S. Hydrogen Sensing Characteristics of Pt−SnO_2 Nano-Structured Composite Thin Films. *J. Mater. Sci.: Mater. Electron.* **2015**, *26*, 3707−3716.
(45) Menumerov, E.; Marks, B. A.; Dikin, D. A.; Lee, F. X.; Winslow, R. D.; Guru, S.; Sil, D.; Borguet, E.; Hutapea, P.; Hughes, R. A.; Neretina, S. Sensing Hydrogen Gas from Atmospheric Pressure to a Hundred Parts per Million with Nanogaps Fabricated Using a Single-Step Bending Deformation. *ACS Sens.* **2016**, *1*, 73−80.
(46) Kocemba, I.; Rynkowski, J. The Influence of Catalytic Activity on the Response of Pt/SnO_2 Gas Sensors to Carbon Monoxide and Hydrogen. *Sens. Actuators, B* **2011**, *155*, 659−666.
(47) Offermans, P.; Tong, H. D.; Van Rijn, C. J. M.; Merken, P.; Brongersma, S. H.; Crego-Calama, M. Ultralow-Power Hydrogen Sensing with Single Palladium Nanowires. *Appl. Phys. Lett.* **2009**, *94*, 223110.

DOI: 10.1021/acsnano.8b02371
ACS Nano 2018, 12, 6079−6088

(48) Yang, F.; Donavan, K. C.; Kung, S. C.; Penner, R. M. The Surface Scattering-Based Detection of Hydrogen in Air Using a Platinum Nanowire. *Nano Lett.* **2012**, *12*, 2924−2930.
(49) Yang, F.; Kung, S. C.; Cheng, M.; Hemminger, J. C.; Penner, R. M. Smaller is Faster and More Sensitive: the Effect of Wire Size on the Detection of Hydrogen by Single Palladium Nanowires. *ACS Nano* **2010**, *4*, 5233−5244.
(50) Xu, T.; Zach, M. P.; Xiao, Z. L.; Rosenmann, D.; Welp, U.; Kwok, W. K.; Crabtree, G. W. Self-Assembled Monolayer-Enhanced Hydrogen Sensing with Ultrathin Palladium Films. *Appl. Phys. Lett.* **2005**, *86*, 203104.

DOI: 10.1021/acsnano.8b02371
ACS Nano 2018, 12, 6079−6088